Research Square

Preprints are preliminary reports that have not undergone peer review.
They should not be considered conclusive, used to inform clinical practice,
or referenced by the media as validated information.

Ultra-Clean Angstroporous Monolayer Amorphous Carbon Yields High Precision Proton Beam

Jiong Lu

chmlujᵉnus.edu.sg

National University of Singapore https://orcid.org/0000-0002-3690-8235

Huihui Lin

Agency for Science, Technology and Research (A*STAR) https://orcid.org/0000-0002-1971-3380

Jian Jiang

City University of Hong Kong https://orcid.org/0000-0002-0579-5194

Yanxin DOU

National University of Singapore https://orcid.org/0000-0002-9183-9164

Pin Lyu

National University Of Singapore

Xiaocang Han

Peking University

Yuan Meng

Peking University

Yuanyuan He

National University Of Singapore

Xin Zhou

National University of Singapore https://orcid.org/0000-0002-6431-731X

Yu Teng

National University of Singapore

Jinxing Chen

National University of Singapore

Yang Meng

National University Of Singapore

Thomas Osipowicz

National University of Singapore

Xiaoxu Zhao

Peking University https://orcid.org/0000-0001-9746-3770

Xiao Cheng Zeng

City University of Hong Kong https://orcid.org/0000-0003-4672-8585

Guoming Lin

National University of Singapore

Kangshu Li

Peking University

Article

Keywords:

Posted Date: April 9th, 2025

DOI: https://doi.org/10.21203/rs.3.rs-5311332/v1

License: This work is licensed under a Creative Commons Attribution 4.0 International License.
Read Full License

Additional Declarations: There is **NO** Competing Interest.

Version of Record: A version of this preprint was published at Nature Nanotechnology on July 28th, 2025. See the published version at https://doi.org/10.1038/s41565-025-01968-3.

Ultra-Clean Angstroporous Monolayer Amorphous Carbon Yields High Precision Proton Beam

Huihui Lin[1, 8], Jian Jiang[2, 3, 8], Yanxin Dou[4, 8], Pin Lyu[1, 8], Xiaocang Han[5], Yuan Meng[5], Yuanyuan He[1], Xin Zhou[1,7],KangShu Li[5], Guoming Lin[1], Yu Teng[1], Jinxing Chen[1], Yang Meng[1], Thomas Osipowicz[4], Xiaoxu Zhao[5], Xiao Cheng Zeng[2, 6*] and Jiong Lu[1, 7*]*

[1] Department of Chemistry, National University of Singapore, Singapore 117543, Singapore

[2] Department of Materials Science and Engineering, City University of Hong Kong, Hong Kong 999077, China

[3] Shenzhen Research Institute, City University of Hong Kong, Shenzhen 518057, China

[4] Centre for Ion Beam Applications, Department of Physics, National University of Singapore, Singapore 117542

[5] School of Materials Science and Engineering, Peking University, Beijing, China

[6] Hong Kong Institute of Clean Energy, City University of Hong Kong, Hong Kong 999077, China

[7] Institute for Functional Intelligent Materials, National University of Singapore, 117544, Singapore

[8] These authors contributed equally: Huihui Lin, Jian Jiang, Yanxin Dou, Pin Lyu

[*]e-mail: xiaoxuzhao@pku.edu.cn; xzeng26@cityu.edu.hk; chmluj@nus.edu.sg

Abstract

Angstrom-scale polygonal rings in monolayer amorphous carbon (MAC) not only tailor its electronic and mechanical properties, but also endow the atomically thin membrane material with diverse angstrom pores for precise regulation of the subatomic species separation and transport, crucial for technological advances across various fields including catalysis, energy devices, and medical applications. However, the lack of industrial-scale synthesis route of intrinsic MAC has severely hindered the progress to harness their versatile angstrom polygons and properties for technological applications that are not offered by the state-of-the-art graphene or bulk amorphous materials. Herein, we report an industry-compatible disorder-to-disorder (DTD) synthetic approach to achieve wafer-scale intrinsic ultra-clean MAC (UC-MAC) within *seconds-timescale*, featuring optimized angstrom polygons without detectable metal contamination and nano-sized pores. Contrary to metal-contaminated MAC, angstroporous UC-MAC enables not only atomic-scale characterization of its intrinsic electronic properties, but also serve as an angstroporous membrane material, enabling the splitting of high-flux H_2^+ ions into a high-precision proton beam with minimal detrimental fragment proton scattering events to date, about twice and 40 times less than those from graphene and commercial carbon thin films, respectively. The membrane with minimum possible material thickness that can yield a highly sharpened proton beam with accurately modulated beam current is desired for proton therapy, especially for non-invasive tumor treatment.

Main

The incorporation of abundant topological structures with non-hexagonal polygonal rings into carbon honeycomb lattices[1] has given rise to a new class of monolayer amorphous carbon beyond graphene[2-4]. This material exhibits tailored electronic and porous properties that distinguish it from both bulk amorphous materials and graphene[1,2,5-16]. Featuring angstrom-scale pores within its 2D carbon network, MAC holds significant promise as an atomically thin membrane material, addressing persistent challenges in the separation and transport of subatomic species and small molecules (Extended Data **Fig. 1**)[17-22], while also serving as a versatile 2D dielectric material with tunable intrinsic electronic properties for ultra-thin flexible electronics[2,5,23,24].

In these disordered 2D systems, randomly oriented, nanometer-sized crystallites composed soley of hexagonal rings are embedded within a continuous polygonal network that contain both hexagonal and non-hexagonal rings, including five-member, seven-member and eight-member rings[16]. Atomically resolved imaging of MAC synthesized *via* laser-assisted chemical vapor deposition (CVD) allows for an in-depth analysis of atomic arrangements in 2D amorphous systems, reinforcing microcrystalline perspectives of glassy solids informed by the competing nanocrystalline model[2,25]. Subsequent investigations linking MAC's atomic configuration to its macroscopic conductivity have yielded valuable insights into the underlying structure-property relationships[3]. Recently, the synthesis of micron-sized nitrogen-doped MAC through solution-phase confined polymerization has opened a new avenue for expanding the library of 2D amorphous materials[4]. Future technological advancements in this field hinge on developing synthetic routes compatible with existing chip manufacturing processes [26-29] for the wafer-scale production of ultra-clean MAC (UC-MAC) with angstrom-scale pores, which is crucial for transitioning laboratory based research into real-world applications. However, the synthesis of such amorphous structures typically occurs under non-equilibrium conditions[30,31], posing a significant challenge in maintaining angstrom-scale pores while ensuring an ultra-clean (metal-free) surface. These issues hinder not only the exploration of their fundamental properties but also the prototype technological

applications that have yet to be demonstrated.

Here, we report an industrial-compatible disorder-to-disorder (DTD) synthesis approach through the combination of nanograin substrate engineering with ICP-CVD method for *seconds-time-scale* growth of 8-inch UC-MAC with near-utility angstrom pores, achieving a growth rate an order of magnitude faster than conventional CVD methods. The atomic structure, intrinsic electronic properties, and angstrom-scale pore characteristics of UC-MAC were symmetrically characterized using a combination of scanning transmission electron microscopy–annular dark field (STEM–ADF) imaging, near-axis scanning transmission ion microscopy (near-axis STIM), and scanning tunneling microscopy (STM) techniques. The presence of tunable non-hexagonal rings in UC-MAC enables regulating the splitting process of hydrogen molecular ions (H_2^+) *through* a high-energy ion nanobeam platform. Our results reveal that ~47 double-proton events can be achieved *via* H_2^+ splitting over UC-MAC, sensing as fine as nearly 50% of double-proton events over graphene. Density functional theory (DFT) calculations reveal that the finer pentagonal and hexagonal rings in UC-MAC are more effective than heptagonal rings and larger rings for splitting H_2^+ ion beams.

Results and discussion

The DTD synthesis of large-area UC-MAC was carried out in a customized industry-compatible fabrication cluster consisting of magnetron sputtering and ICP-CVD growth chambers, which is fully compatible with existing semiconductor fabrication technique[26,32]. Our synthesis strategy begins with the implementation of magnetron sputtering technique to engineer the copper thin film on sapphire or SiO_2/Si wafer characterized by abundance of irregular nanograins with a density of approximately 2260 ± 20 /um^2 (termed as Disorder-Sub). The formation of nanograins is determined by the substrate temperature and metal sputtering rate, with the detailed experimental parameters provided in Supplementary **Tab. 1**. Low-magnification TEM images and false-colored TEM images of different Disorder-Subs, including Pt, Co, and CuNi Disorder-Subs, are shown in Supplementary **Fig.**

1, revealing irregular grains with sizes of several tens of nanometers. This is achieved by the magnetron-assisted deposition of metal species on SiO_2/Si wafer at low temperature of 200 °C, as revealed by AFM phase images (Cu substrate #1, Extended Data **Fig. 2a, b**)[27,33,34]. Unlike the low nucleation density with uniform grain orientation observed for SCG growth on single-crystal substrates (Supplementary **Fig. 2a**)[35-37], the Disorder-Sub can be viewed as the coalescence of numerous nanoscale crystalline grains (nanograins) into a thin-film structure, as shown in Extended Data **Fig. 2a, b** and Supplementary **Fig. S3d-f**. Graphene grains grown on these nanograins could exhibit varied orientations (Supplementary **Fig. 2b**). Togather with the plasma effect, such unique substrate structure promotes a sufficiently high nucleation density, even under high-temperature growth conditions, ultimately enabling the successful synthesis of UC-MAC. The use of Disorder-Sub support significantly increases the nucleation density, which was confirmed by comparing the growth of mosaic nanocrystalline graphene (n-G) on two Cu substrates with different grain sizes (Extended Data **Fig. 2** for detailed description). The growth and coalescence of mis-aligned nanometer-sized domain over Disorder-Sub enables a controllable formation of densely populated angstrom-scale hexagonal and non-hexagonal rings in the MAC. Combining this Disorder-Sub strategy with ICP-CVD synthesis at high temperature of 820 °C concurrently boosts the nucleation density while maintaining surface cleanliness, thereby facilitating the growth of UC-MAC for regulating H_2^+ splitting (**Fig. 1a**). In contrast, current CVD synthesis of MAC on commercial Cu foils is often performed at relatively low temperature, typically below 500 °C (Supplementary **Tab. 2**). This may lead to the formation of large voids, presumably due to incomplete growth and significant thermal expansion coefficient mismatches between the MAC film and the copper foil substrate. Additionally, the unpredictable adhesion of reactive metal particles to the disordered surface of the carbon film further prevents the fabrication of UC-MAC.

Fig. 1b-d reveals the entire DTD growth process of UC-MAC together with a sample transfer of an 8-inch film onto SiO_2 substrates. Optical image of MAC transferred on SiO_2 substrate shows a uniform and homogeneous film (**Fig. 2a**). The corresponding AFM imaging reveals

an ultra-clean surface and an apparent thickness of ~0.9 nm for our MAC (**Fig. 2b**), consistent with the measured thickness of monolayer carbon films[2,38]. STEM-ADF cross-sectional imaging reveals a 0.46-nanometer-thick of MAC, further suggesting its monolayer structure (Extended Data **Fig. 3**). In contrast to high quality graphene, MAC exhibits a negligible intensity of Raman 2D band at approximately 2670 cm^{-1}, with a D to G band intensity ratio of $I_D/I_G \sim 0.71$ (Supplementary **Fig. 3a-b**). This suggests a high non-hexagonal rings density and a lack of long-range order in MAC[2,3]. Another advantage of our DTD synthesis method is the dramatically enhanced nucleation density, which effectively increases the growth efficiency of MAC. As illustrated in Extended Data **Fig. 4a–b**, we achieved ultra-fast MAC growth within 3 seconds, more than an order of magnitude (>20 times) faster than traditional CVD growth of MAC or amorphous hBN (**Fig. 2c** and Supplementary **Tab. 2**). Without using Disorder-Sub substrate, graphene grown on as-sputtered Cu (111) single crystal[28,39] (details of as-sputtered Cu (111) single crystal seen in Extended Data **Fig. 4e–f**), even after 100 s, only forms an incomplete film (Extended Data **Fig. 4g-j**). Apart from the growth efficiency, this DTD synthesis can be further extended to other metal Disorder-Sub beyond copper including platinum, cobalt, and copper/nickel alloy Disorder-Subs (Supplementary **Fig. 1** and Extended Data **Fig. 4d**). Moreover, the DTD growth method can be empolyed to fabricate other 2D disorder materials beyond carbon (eg. nanocrystalline α-Mo_2C film), as demonstrated in Extended Data **Fig. 5**.

The as-prepared UC-MAC *via* DTD synthesis exhibits near-utility angstrom-sized hexagonal and non-hexagonal rings, with the absence of detectable metal contaminations. This enables direct visualization of their atomic structure and local electronic structure using STEM and STM techniques. The selected area electron diffraction (SAED) reveals diffuse halos and the absence of diffraction spots, suggesting that UC-MAC has an amorphous nature (**Fig. 2d-e**)[2]. This is further supported by STEM-ADF imaging, which reveals a significant portion of randomly-arranged non-hexagonal rings in UC-MAC (**Fig. 2f**). The C 1*s* XPS spectra of UC-MAC reveals a predominant sp^2 peak (Supplementary **Fig. 4a**), consistent with previously reported work[2]. Notably, no detectable Cu 2*p* signal is observed from UC-MAC

(Supplementary **Fig. 4b**). Core-loss EELS spectrum further confirms the absence of metal contamination in the films, as shown in Supplementary **Fig.5**. Additionally, STM image of the UC-MAC transferred onto highly oriented pyrolytic graphite (HOPG) reveals disordered bright protrusion patterns (**Fig. 2g**) distinct from those observed in graphene[40]. Zoom-in STM images of local regions taken at different bias voltages further highlight the localization of wavefunctions in UC-MACs for both filled and empty states, as reflected by their characteristic nodal patterns in d*I*/d*V* maps (**Fig. 2h-i**). The absence of detectable residues and structural deformations in the UC-MAC transferred onto HOPG across various scales was confirmed using techniques including optical microscope, AFM and STM/STS analyses, as shown in Supplementary **Fig. 6** and Extended Data **Fig. 6**. Given the disordered nature of UC-MAC, the d*I*/d*V* measurements show site-dependent spectral features and quasi-particle energy gaps. A statistical analysis of over 50 spectra at different sites, revealing a variation of quasi-particle energy gaps ranging from 80 meV to 910 meV, with an average value of around 422±23 meV (**Fig. 2j** and Extended Data **Fig. 6**). This value is much smaller than the energy gap of MAC reported in previous studies, likely due to the surface cleanliness of UC-MAC materials, which allows for a direct evaluation of their intrinsic local electronic structures. A detailed explanation of the determination of the energy gap from STS measurements are shown in Supplementary **Fig. 7**. The presence of sizeable gap feature in UC-MAC films makes them promising 2D semiconductors candidates for assembling sub-2nm semiconductor integrated devices in the post-Moore's law era[41].

Using the DTD synthesis, we can grow monolayer carbon films with tunable macroscopic properties ranging from mosaic ultra-clean nanocrystalline graphene (n-G) to UC-MAC on Disorder-Sub (**Fig. 3**). This is achieved by controlling the ICP power (20-100W) to regulate the number of radicals generated from carbon sources, combined with the use of Cu Disorder-Subs, enabling fine-tuning of the nucleation density. The growth at ICP power of 20 W yields a low density of non-hexagonal rings in ultra-clean n-G, resulting in the formation of mosaic domain-like patterns separated by grain boundaries (**Fig. 3a-b**, **3d-e)**. Increasing the ICP power to 100 W enhances the concentration of carbon radical species derived from

CH_4 gas, which in turn increases the nucleation density. This leads to a higher density of non-hexagonal rings, resulting in the formation of UC-MAC with an ultrafast growth time of just 3 seconds (**Fig. 3c, f**). It is also observed that the synthesized UC-MAC comprises Zachariasen-continuous random networks (Z-CRNs) and crystallite regions (**Fig. 3c, f**). The Z-CRN region features pentagonal, isolated hexagonal, heptagonal, and octagonal member rings, while the crystalline region consists of hexagonal rings surrounded by six other hexagons, or those larger than this arrangement[2,3]. As shown in **Fig. 3h-i**, the distribution of angles and bond lengths in UC-MAC (83–154°; 0.9–2.1 Å) is much broader than that of single-crystal graphene (SCG) grown on Cu foils (120°; 1.4 Å)[1,42] and as-grown mosaic n-G, indicating a high degree of structural distortion[2,3,19]. Additionally, the growth of such UC-MAC can be well controlled with high reproducibility as verified by multiple STEM-ADF images of ultra-clean n-G and MAC samples synthesized under different batches (Extended Data **Fig. 7)**. The continuity and glassy structures of two representative films (#1) and 8 inch UC-MAC (#2) were further confirmed through a series of characterizations, with detailed information provided in Supplementary **Fig. 5,** Supplementary **Fig. 8 to** Supplementary **Fig. 16**. Furthermore, based on tests conducted at 10 randomly selected sites (Supplementary **Fig. 3c**), UC-MAC exhibits the characteristic macroscopic electrical uniformity with a resistance of about 95.7 GΩ, consistent with the value reported previously[2].

Leveraging its ultra-clean surface and the properties of angstrom pores, we further demonstrated the unique capability of UC-MAC as membrane material to modulate the splitting of H_2^+ ions to generating high-precision proton beams. The use of MAC to generate a more sharpened high-energy proton beam enables more precise proton therapy in treating tumors, especially those located in delicate organs[43]. Accelerating H_2^+ instead of proton is considered a promising solution to reduce the space charge effect for delivering a proton beam current that is an order of magnitude higher than in existing cyclotrons[44]. High current proton beams provide a powerful tool for proton therapy[43], medical isotope production[45] and neutrino physics[46]. Previously, ultra-thin commercial carbon films have been utilized as membrane material for proton generation, through the dissociation of H_2^+ without altering the

state of the high-current H_2^+ accelerator[44]. The thickness and polygonal ring pattern of the membrane material affects both its lifespan and the quality of the extracted proton beam (Supplementary **Fig. 17**). Therefore, controlling the splitting process of H_2^+ ions requires the capability of precise tailoring of atomic structures of carbon films with reduced thickeness, small polygonal rings, and impeccable surface cleanliness. As-grown ultra-clean monolayer carbon with tunable atomic structures, including UC-MAC and SCG (as a reference sample shown in Supplementary **Fig. 18**), can serve as the ideal membrane-material platform to regulate the proton beam quality *via* the splitting of H_2^+ ions, as illustrated in **Fig. 4a**. The process initiates with a radio frequency field ionizing a hydrogen molecule, causing it to shed an electron and transform into a H_2^+ ion. In this state, two protons share a single electron, forming a chemical bond that maintains the molecular structure. Utilizing an acceleration field and focusing system, a high-energy H_2^+ nanobeam is generated and directed towards a freestanding 2D crystal, culminating in splitting (detial parameters of high-energy H_2^+ nanobeam as shown in Supplementary **Fig. 19**). **Fig. 4b** shows an optical microscopic image of freestanding UC-MAC transferred on an Au grid. Our near-axis STIM technique can visualize the UC-MAC with an enhanced contrast compared to empty regions (marked by pink and Macaron blue arrows in **Fig. 4c**). The optical microscopic and near-axis STIM images of ultra-clean SCG are depicted in Supplementary **Fig. 20**. Our high energy ion nanobeam, as detailed in Extended Data **Fig. 8**, enables precise modulation of the interaction between the electron cloud density of the monolayer carbon and the H_2^+ ions. This interaction results in the formation of ~47 double-proton events (**Fig. 4d**), an ultra-fine sensitivity that is significantly more sensitive (~46 times) than that of commercially available thin carbon film (~8 nm). In addition, the double proton events in **Fig. 4d**, originating from the scattering of fragment protons, which are used to analyze the differences in fragment proton scattering in different cases. Additionally, the commercial available thin SiN films (10 nm~100 nm) reduce the proton beam quality with noticeable fragment proton scattering (Supplementary **Fig. 17a**), a challenge that can be mitigated by using UC-MAC. However, when MAC surfaces are modified with metal (Cu) atoms/clusters at a low growth temperature of 460 °C (Supplementary **Fig. 21**), the double-proton events surge to approximately 123 arbitrary unit

(**Fig. 4d**), even surpassing that of ultra-clean SCG. This upsurge is likely due to the enlarged scattering cross-section of fragment protons from the metal impurities. In contrast, the number of double-proton events from the UC-MAC is found to be lower than that from ultra-clean SCG, further highlighting the essential role of surface cleanliness in UC-MAC for regulating H_2^+ ion splitting. By employing UC-MAC as a stripping foil, we have achieved a precise control over H_2^+ splitting into protons, yielding much lesser scattered fragment proton events due to its finer sensitivities, comparable to about 50% of those obtained with SCG (**Fig. 4d**). Apart from the superior quality of the proton beam obtained, the proton beam quantity from H_2^+ splitting can be precisely controlled using UC-MAC, showcasing yields ranging from 88.8±3.2 to 296.0±4.1 proton events per second per detector (**Fig. 4e**).

We further elucidate the mechanism of the splitting of the high-energy H_2^+ ions with the SCG/UC-MAC monolayer, especially the role of the polygonal carbon structure. The constrained Density Functional Theory (cDFT) calculations were applied to investigate the electron transfer from H_2^+ ions to the MAC/SCG monolayer during the molecular ion splitting process (see Methods). The splitting of high-energy H_2^+ ions into protons upon pentrating SCG/UC-MAC monolayer is a complex process, where the interaction between the molecular ion and the unique polygonal carbon structure plays a central role. The SCG/UC-MAC monolayer, composed of carbon atoms arranged in pentagonal, hexagonal, and heptagonal rings, creates diverse electrostatic environment and potential energy landscapes. The different polygonal structural features enable distinct interaction with the passing H_2^+ ions. The cDFT calculations reveal that as H_2^+ ions approach the monolayer, partial electron transfer occurs. This charge redistribution destabilizes the covalent bond between the two hydrogen atoms, setting the stage for the bond breaking.

The energy profile for H_2^+ penetration depends on the molecular ion's orientation with respect to the monolayer (i.e., H-H bond being in perpendicular- or parallel-configuration). In the vertical orientation (**Fig. 4f**), where the H-H bond is perpendicular to the monolayer, the leading H atom (denoted as H_B in **Fig. 4f** lower panel) nearby either pentagonal, hexagonal, or heptagonal ring, encountering relatively lower activation energy of 3.3–4.4 eV as the first

step (Supplementary **Fig. 22**). The splitting of the two hydrogen atoms occurs as both pass through the monolayer, a next step that would encounter higher activation energy, depending on the ring type. The activation energies follow the trend , $E_5 > E_6 > SE > E_7$ with subscript of E_5, E_6, and E_7 corresponding to pentagonal, hexagonal, and heptagonal ring, respectively (**Fig. 4i and** Supplementary **Fig. 23**). Both activation energies of E_5 and E_6 are higher than the splitting energy (*SE)* of H_2^+, where *SE* = ~15.6 eV (see horizontal dashed line in **Fig. 4i**). This indicates an energy conversion pathway where kinetic energy is transferred to internal potential energy, further promoting splitting of H_2^+ and free-moving protons. The higher activation energy in the later step results in a strong pulling force to seperate H_A and H_B apart when the two are located on opposite sides of the monolayer.

In contrast, a mostly identical activation energy (52.9 ~ 55.3 eV) was obtained in H-H bond parallel-configuration penetration, as shown in **Fig. 4j** and Supplementary **Fig. 24**. As depicted in **Fig. 4g-h**, the energy barrier of H_2^+ splitting diminishes when the hydrogen molecular ion approaches the SCG/MAC monolayer vertically, promoting H atoms separation due to the strong interaction with SCG/MAC monolayer, whereas there remained an activation energy for splitting of neutral H_2 molecule as a comparison, as shown in Extended Data **Fig. 9**. In addition, charge analysis showed that the H atom becomes more positively charged when approaching the SCG/MAC monolayer more closely as shown in Supplementary **Fig. 25**. Furthermore, machine-learning-potential-based molecular dynamics simulations were performed based on the binary step and the linear electron transfer models (see Method), confirming the splitting of H_2^+ (**Movie 1** and **2**) moving through the SCG/MAC. When the distance between H_A and H_B exceeds 4.2 Å, the convalent bond between them breaks[47], causing the two covalent-bonded H atoms in the high-energy H_2^+ split into two protons and sequentially pass through the monolayer carbon film separately. The higher density of heptagonal ring defects in UC-MAC can result in a smaller effective area. In view of $E_7 < SE$ (as marked by a red cross in **Fig. 4i**), the presence of heptagonal ring defects in UC-MAC can result in a smaller effective unit area for H_2^+ splitting compared to the SCG, consistent with the collected proton signal in **Fig. 4d**. Apart from the surface cleanness, another key aspects to acheving the precise H_2^+ splitting requires the preventation

of large-pores in UC-MAC since large pore sizes lack controllability and can also lead to higher edge energies. For example, the edge energy for graphene nanoribbons has been computed to be 1.24 eV/Å and 1.53 eV/Å for armchair and zigzag edges, respectively[48], which likely inhibits the formation of large pores in MAC. We further examine the formation energy of various pores or defects in MAC (**Fig 3j** and Supplementary **Fig. 26**). The largest observed pores resemble those formed by four carbon atom vacancies (Supplementary **Fig. 26o**, **Fig. 3c, f**, and Extended Data **Fig. 7c, f**). This suggests that the DTD method effectively suppresses the formation of large pores with formation energies greater than 0.11 eV per atom and areas exceeding 20 $Å^2$. These findings highlight the ability of the DTD method to precisely control the formation of angstrom-scale pores, ensuring the creation of ultraclean 2D amorphous materials with well-regulated pore sizes. The reduced double proton events in UC-MAC demonstrate its superior ability to minimize proton scattering compared to commercial materials, likely due to its small scattering cross-section. Additionally, it offers finer control over H_2^+ splitting than the SCG, owing to its optimized polygonal ring distribution, which effectively regulates H_2^+ splitting in the vertical direction relative to UC-MAC. Previous studies have shown that the strain and curvature of defect-free graphene demonstrate a high proton permeation rate through an ambient-condition, low-energy catalytic mechanism[18,21,49]. However, such mechanisms differ fundamentally from the high-energy, non-equilibrium H_2^+ splitting observed in our study. Such remarkable performance would be impossible without ultra-clean MAC featuring optimized angstrom-scale polygons. Large pores beyond the angstrom scale would permit H_2^+ ion transport without splitting into protons, while metal contamination in MAC would significantly increases undesired proton scattering events, as revealed in our study.

Conclusion

In summary, we demonstrate an ultra-fast industry-compatible disorder-to-disorder synthesis approach for fabricating the 8-inch intrinsic UC-MAC, with no detectable metal particle impurities or large pore, highlighting its prototype technological application as membrane

material for regulating the splitting of high-energy H_2^+ into protons. UC-MAC enables finer-controlling the H_2^+ splitting to yield a high-precision proton beam with minimal fragment proton scattering, outperforming the state-of-the-art graphene and bulk commercial carbon thin films. The robust atomically thin membrane that produces a highly sharpened proton beam with accurately modulated beam current is essential for proton therapy, particularly for non-invasive tumor treatment. Furthermore, achieving wafer-scale manufacturing of industrial-grade 2D amorphous materials is critical for advancing technologies in catalysis, energy devices, and medical applications.

Methods

Growth of UC-MAC through industry-compatible disorder-to-disorder synthesis

UC-MAC is grown using a disorder-to-disorder synthesis within a customized, industry-compatible fabrication cluster that incorporates magnetron sputtering and ICP-CVD growth chambers. Initially, a magnetron sputtering method is employed to deposit metal Disorder-Sub onto 8-inch sapphire or SiO_2/Si substrates. Prior to sputtering, the chamber is evacuated to a pressure of approximately 1 x 10^{-6} Pa and maintained for 60 minutes. This is followed by a pre-sputtering of the metal targets, all of which are of high purity (>99.99% atomic) and commercially sourced. This pre-sputtering step helps eliminate surface contamination before the deposition process. Standard sputtering conditions include a substrate temperature of 200°C, a deposition rate of 0.1 Å/s, and a chamber pressure of 30 mTorr. The grain of the substrate is effectively regulated by the temperature of the support substrate (200 °C ~ 800 °C) and the thickness of the sputtered film (100 nm ~ 1500 nm). Subsequently, the Disorder-Sub obtained from sputtering are transferred to the ICP-CVD chamber through a loadlock chamber for the growth process. The growth substrates are rapidly heated to 820°C for a few seconds. The growth parameters are set at a temperature of 820°C, a pressure of 50 mTorr, a CH_4/H_2 ratio of 1:15, a plasma power of 20~100 W, and a growth duration ranging from 3 to 20 seconds. Post-growth, the samples are quickly cooled by lifting the heating stage away from the heating wire.

For the tailored growth of nanocrystalline α-Mo_2C films on Cu Disorder-Sub, the process involves replacing conventional metal growth substrates with multilayer Disorder-Subs (Extended Data **Fig. 5a**). Initially, Cu Disorder-Sub is sputtered onto SiO_2/Si substrates following the standard preparation method for Cu Disorder-Sub. Next, Mo films are sputtered onto the Cu Disorder-Sub. Standard sputtering conditions include a substrate temperature of 200°C, a deposition rate of 0.1 Å/s, and a chamber pressure of 50 mTorr. The sputtered multilayer metal substrates is then transferred to the ICP-CVD chamber through a load-lock chamber for the growth process. The growth substrates are rapidly heated to 850°C for a few seconds. The growth parameters are set at a temperature of 850°C, a pressure of 50 mTorr, a

CH_4/H_2 ratio of 1:10, a plasma power of 100 W, and a growth duration of approximately 100 seconds. The strong chemical interaction between carbon radicals generated from CH_4 plasma with the Disorder-Sub leads to the transformation of the Mo films into transition metal carbide films (Extended Data **Fig. 5a)**. Note: In conventional methods, α-Mo_2C films exhibit strong interactions with the substrate. In our case, the as-grown α-Mo_2C films can be easily transferred to other substrates by etching the underlying Cu Disorder-Sub, showcasing significant potential in practical applications. This method facilitates precise control over the deposition and growth phases, ensuring the production of high-quality, specialized nanocrystalline transition metal carbide films.

Transfer processing of UC-MAC. During the PECVD growth process, protons can penetrate through single-layer carbon membranes (graphene or MAC), forming H_2, which decouples the single-layer carbon membrane from the substrate[39,50]. The weak interaction between graphene and the underlayer substrate facilitates the removal of surface residues that are typically introduced during the transfer process[39,51]. After completing the sample growth, polymethyl methacrylate (PMMA, 996 kDa, 4 wt% solution in ethyl lactate) is spin-coated onto the as-grown film at 2000 rpm for 1 minute, followed by baking at 180 °C for 3 minutes. The growth metal substrates are then etched using a 0.2 M ammonium persulfate ($(NH_4)_2S_2O_8$) aqueous solution. The as-grown samples are subsequently transferred to other substrates or TEM grids and allowed to air-dry. The sample is sequentially washed with acetone and isopropanol to remove the PMMA and any residues. Before measurements, the as-transferred sample is annealed at 350 °C under high vacuum (~10^{-5} Pa) for 2 hours to eliminate possible surface adsorbates and contaminants.

Splitting of hydrogen molecular ions experiments. A high energy ion nanobeam, which is able to shape an ion beam at sub-10 nm scales[52], offers fast hydrogen molecular ions bomdarding freestanding 2D materials. The high energy ion nanobeam, also named nuclear nanoprobe, primarily consists of a 3.5 MV Singletron accelerator with a beam energy stability of ±50 eV over 5 h, a focusing lens syetem using a spaced Oxford triplet configuration, an

electrostatic scanning system with 16 bits resolution, a closed loop nano-positioning stage with a 4 nm resolution and a data acquisition system with more than 50 kHz pixel update time. A 1.5 million-electron-volt (MeV) ion beam is focused to a width of less than 200 nm (much smaller than the freestanding 2D materials size), as shown in Supplementary **Fig. 19b-c**. Typical measured beam current stabilities for 1.5 MeV H_2^+ experiments are shown in Supplementary **Fig. 19a** and Extended Data **Fig. 8b, c**. Near-axis scanning transmission ion microscopy[52] technology is a sensitive method to measure the splitting of hydrogen molecular ions bombarding on freestanding membranes. Here, we further develop the near-axis scanning transmission ion microscopy technology for fragment proton scattering analysis. Because beam current stabilities are controled less than 10 %, double-proton events measured on near-axis position (collect time: 20 seconds) are an suitable indicator for the splitting of hydrogen molecular ions and fragment proton scattering. And one double-proton event represents two protons signal detected from single H_2^+ ion.

Characterizations. Atomic-resolution STEM-ADF imaging was performed on an aberration-corrected JEOL ARM200F, equipped with a cold field-emission gun and an ASCOR corrector operating at 60 kV. Raman spectra were performed using a Witec/alpha 300 R confocal microscope with a 532 nm laser at atmospheric conditions. The laser powers are lower than 1 mW during the measurements. AFM images were taken using the Bruker Dimension Icon in tapping mode. The superconducting and transport properties are carried out in ^{4}He cryostat with a superconducting magnet (Oxford Teslatron 8T) with currents of 1~10 μA. For most transport properties measurements, four-probe contacts are used by e-beam evaporated 80 nm Cr/Au array (200 μm dots with 500 μm spacing).

STM/STS Measurements. The STM/STS measurements were conducted in an LT-STM instrument held at 4.5 K and 77 K with a base pressure lower than 10^{-10} mbar. The STM tip was calibrated spectroscopically on Au(111) substrate. All of the dI/dV spectra were measured through a standard lock-in technique with a modulated voltage of 5 to 20 mV at a frequency of 812 Hz.

Constrained density functional calculation. The cDFT was adopted to investigate the positively charged hydrogen molecular ions passing through a SCG/MAC monolayer. The hydrogenated graphene and hydrogenated graphene ($C_{24}H_{12}$) with a Stone-Wales defect, as two model systems, were used to investigate the non-hexagonal effect on the splitting of hydrogen molecular ions. The hydrogen molecular ions were initially placed 5 angstroms away from the membrane. Three constraint states were adopted to study different stages of electron transfer to the membrane during the splitting: (1) The initial state, where the sum charge of hydrogen molecular ions (with two H atoms being named as H_A and H_B) was set to be one ($C_A + C_B = 1$); (2) the second state, where the charge of H_B atom was set to be one ($C_B = 1$); and (3) the final state where the sum charge of hydrogen molecular ions was set to be two ($C_A + C_B = 2$). The constrains were applied based on the Löwdin population. The lower limit of energy barrier for the second step H_2^+ splitting was defined as the energy difference between the transition state of the constraint-(3) and the initial state of the constraint-(3). The upper limit of energy barrier for H_2^+ splitting was defined as the energy difference between the transition state of the constraint-(3) and the initial state of the constraint-(2). The cDFT calculation was employed using the NWChem[53] package, for which the B3LYP functional was adopted[54].

Molecular dynamics simulations. First, a machine learning potential (MLP) model was trained using the force data derived from the cDFT calculations for the subsequent molecular dynamics simulation. The architecture of the MLP contained a 128-node hidden layer neural network using the Rectified linear unit (ReLU) as the activation function. The MLP model was built using the PyTorch library.[55] The root mean square error (RMSE) of force prediction was obtained to be 146 and 194 meV/ Å for the MLP trained based on linear model and the binary step model, respectively, as shown in Supplementary **Fig. 27**, demonstrating the accurate force prediction by using the MLP. The linear and binary step of electron transfer model was described as two different electron pathways (see (1) and (2) below).

Second, the molecular dynamics simulation was performed using a custom-made code for integrating Newton's equations of motion. An adaptive timestep scheme was employed with a maximum timestep of 10 attoseconds, and no thermostat was used due to the extremely short duration of hydrogen molecular ions moving through the membrane. Two simplified electron pathways were considered: (1) An electron was transferred to the SGC/MAC monolayer (membrane) immediately as frontend H_B passing through the SGC/MAC monolayer, as shown in Supplementary **Fig. 28a**. (2) The charge of the molecular hydrogen ion changed linearly as frontend H_B approached to the SGC/MAC monolayer, depicted in Supplementary **Fig. 28b**.

Acknowledgements

J.L. acknowledges support from the NRF, Prime Minister's Office, Singapore, under the Competitive Research Program Award (NRF-CRP29-2022-0004), and MOE Tier 2 grants (MOE-T2EP10221-0005, MOE-T2EP10223-0004, MOE-T2EP10124-0004). X.C.Z. acknowledges the support from the Hong Kong Global STEM Professorship Scheme and the Research Grants Council of Hong Kong (GRF Grant No. 11204123). J.J. acknowledges the funding support the National Natural Science Foundation of China (Grant No. 22303072). X.X.Z. thanks the National Key R&D Program of China (2024YFE0109200), the Beijing Natural Science Foundation (JQ24010, Z220020), and the National Natural Science Foundation of China (52273279).

Contributions

J. Lu supervised the project. H. Lin. and J. Lu organized the collaborations and conceived the experiments. H. Lin. performed the Disorder-Sub deposition, the disorder-to-disorder synthesis, structural characterization and electrical measurements of UC-MAC. P. Lyu performed the STM/STS characterization of MAC. Y.X. Dou, H. Lin. and T.O. performed the single hydrogen molecular ion splitting experiment and data analysis. X.C.Han, Yuan M., K.S. Li and X.X. Zhao. performed the STEM/EELS experiments and data analysis. X. Zhou performed the SAED characterizations of SCG. G.M. Lin performed the TEM/SAED

characterizations of Disorder-Subs. J. Jiang performed the density functional theory calculations and other theoretical calculations under the supervision of X.C.Zeng. H. Lin and J. Lu wrote the manuscript with input from X.C. Zeng, J. Jiang, Y.X. Dou and X.X. Zhao. All the authors contributed to the scientific discussion.

Conflict of Interest

The authors declare no conflict of interest.

References

1 Novoselov, K. S. *et al.* Electric field effect in atomically thin carbon films. *science* **306**, 666-669 (2004).

2 Toh, C.-T. *et al.* Synthesis and properties of free-standing monolayer amorphous carbon. *Nature* **577**, 199-203 (2020).

3 Tian, H. *et al.* Disorder-tuned conductivity in amorphous monolayer carbon. *Nature* **615**, 56-61 (2023).

4 Bai, X. *et al.* Nitrogen-doped amorphous monolayer carbon. *Nature*, doi: 10.1038/s41586-41024-07958-41580 (2024).

5 Hong, S. *et al.* Ultralow-dielectric-constant amorphous boron nitride. *Nature* **582**, 511-514 (2020).

6 Deringer, V. L. *et al.* Bonding nature of local structural motifs in amorphous GeTe. *Angew. Chem. Int. Ed.* **53**, 10817-10820 (2014).

7 Deringer, V. L. *et al.* Origins of structural and electronic transitions in disordered silicon. *Nature* **589**, 59-64 (2021).

8 Li, Z. *et al.* Ultrastrong conductive in situ composite composed of nanodiamond incoherently embedded in disordered multilayer graphene. *Nat. Mater.* **22**, 42-49 (2023).

9 Kim, M. *et al.* 2D Materials in the display industry: status and prospects. *Adv. Mater.* **35**, 2205520 (2023).

10 Kim, K. *et al.* Ultralow-k amorphous boron nitride film for copper interconnect capping layer. *IEEE Trans. Electron Devices* **70**, 2588-2593 (2023).

11 Guo, J. *et al.* Hypocrystalline ceramic aerogels for thermal insulation at extreme conditions. *Nature* **606**, 909-916 (2022).

12 Liu, W. *et al.* A solution-processable and ultra-permeable conjugated microporous thermoset for selective hydrogen separation. *Nat. Commun.* **11**, 1633-1640 (2020).

13 Tan, C. K. Y., Fu, W. & Loh, K. P. Polymorphism and ferroelectricity in indium (III) selenide. *Chem. Rev.* **123**, 8701-8717 (2023).

14 Louro, C., Oliveira, J. C., Chhowalla, M. & Cavaleiro, A. Silicon effect on the hardness of rf sputtered B–C: Si amorphous films. *Plasma Process. Polym.* **6**, S141-S145 (2009).

15 He, Y. *et al.* Amorphizing noble metal chalcogenide catalysts at the single-layer limit

towards hydrogen production. *Nat. Catal.* **5**, 212-221 (2022).
16 Joo, W.-J. *et al.* Realization of continuous Zachariasen carbon monolayer. *Sci. Adv.* **3**, e1601821 (2017).
17 Wang, J. *et al.* Cascaded compression of size distribution of nanopores in monolayer graphene. *Nature* **623**, 956-963 (2023).
18 Sun, P. *et al.* Limits on gas impermeability of graphene. *Nature* **579**, 229-232 (2020).
19 Griffin, E. *et al.* Proton and Li-ion permeation through graphene with eight-atom-ring defects. *ACS Nano* **14**, 7280-7286 (2020).
20 Lozada-Hidalgo, M. *et al.* Sieving hydrogen isotopes through two-dimensional crystals. *Science* **351**, 68-70 (2016).
21 Wahab, O. *et al.* Proton transport through nanoscale corrugations in two-dimensional crystals. *Nature* **620**, 782-786 (2023).
22 Sun, P. *et al.* Exponentially selective molecular sieving through angstrom pores. *Nat. Commun.* **12**, 7170-7176 (2021).
23 Huang, J.-K. *et al.* High-κ perovskite membranes as insulators for two-dimensional transistors. *Nature* **605**, 262-267 (2022).
24 Fanchini, G., McCauley, J. W. & Chhowalla, M. Behavior of disordered boron carbide under stress. *Phys. Rev. Lett.* **97**, 035502 (2006).
25 Koga, K., Tanaka, H. & Zeng, X. First-order transition in confined water between high-density liquid and low-density amorphous phases. *Nature* **408**, 564-567 (2000).
26 Thomas, S. An industry view on two-dimensional materials in electronics. *Nat. Electron.* **4**, 856-857 (2021).
27 Gao, L. *et al.* Face-to-face transfer of wafer-scale graphene films. *Nature* **505**, 190-194 (2014).
28 Chen, T.-A. *et al.* Wafer-scale single-crystal hexagonal boron nitride monolayers on Cu (111). *Nature* **579**, 219-223 (2020).
29 Wan, Y. *et al.* Wafer-scale single-orientation 2D layers by atomic edge-guided epitaxial growth. *Chem. Soc. Rev.* **51**, 803-811 (2022).
30 Liu, D. *et al.* Raman enhancement on ultra-clean graphene quantum dots produced by quasi-equilibrium plasma-enhanced chemical vapor deposition. *Nat. Commun.* **9**, 193 (2018).
31 Lin, H. *et al.* Growth of environmentally stable transition metal selenide films. *Nat. Mater.* **18**, 602-607 (2019).
32 Shi, L. Challenges remain for 2D semiconductor growth. *Nat. Nanotechnol.* **19**, 145-145 (2024).
33 Huang, P. Y. *et al.* Grains and grain boundaries in single-layer graphene atomic patchwork quilts. *Nature* **469**, 389-392 (2011).
34 Paredes, J., Villar-Rodil, S., Solís-Fernández, P., Martínez-Alonso, A. & Tascon, J. Atomic force and scanning tunneling microscopy imaging of graphene nanosheets derived from graphite oxide. *Langmuir* **25**, 5957-5968 (2009).
35 Lee, J.-H. *et al.* Wafer-Scale Growth of Single-Crystal Monolayer Graphene on Reusable Hydrogen-Terminated Germanium. *Science* **344**, 286 (2014).
36 Luo, D. *et al.* Adlayer‐free large‐area single crystal graphene grown on a Cu (111) foil. *Adv. Mater.* **31**, 1903615 (2019).

37 Wang, M. *et al.* Single-crystal, large-area, fold-free monolayer graphene. *Nature* **596**, 519-524 (2021).
38 Liu, Y. *et al.* Giant enhancement in vertical conductivity of stacked CVD graphene sheets by self-assembled molecular layers. *Nat. Commun.* **5**, 5461 (2014).
39 Yuan, G. *et al.* Proton-assisted growth of ultra-flat graphene films. *Nature* **577**, 204-208 (2020).
40 Lu, J., Neto, A. C. & Loh, K. P. Transforming moiré blisters into geometric graphene nano-bubbles. *Nat. Commun.* **3**, 823 (2012).
41 Jiang, J., Wu, P., Liu, Y., Kong, J. & Peng, L.-M. Towards fab-compatible two-dimensional electronics. *Nature Reviews Electrical Engineering* (2025).
42 Niu, T., Zhou, M., Zhang, J., Feng, Y. & Chen, W. Growth intermediates for CVD graphene on Cu (111): carbon clusters and defective graphene. *J. Am. Chem. Soc.* **135**, 8409-8414 (2013).
43 Bortfeld, T. R. & Loeffler, J. S. Three ways to make proton therapy affordable. *Nature* **549**, 451-453 (2017).
44 Alonso, J. R., Barlow, R., Conrad, J. M. & Waites, L. H. Medical isotope production with the IsoDAR cyclotron. *Nat. Rev. Phys.* **1**, 533-535 (2019).
45 Weidner, J. *et al.* Proton-induced cross sections relevant to production of ^{225}Ac and ^{223}Ra in natural thorium targets below 200 MeV. *Appl. Radiat. Isot.* **70**, 2602-2607 (2012).
46 Winklehner, D. *et al.* High intensity cyclotrons for neutrino physics. *Nucl. Instrum. Methods Phys. Res., Sect. A* **907**, 231-243 (2018).
47 Xu, H. *et al.* Observing electron localization in a dissociating H_2^+ molecule in real time. *Nat. Commun.* **8**, 15849 (2017).
48 Jun, S. Density-functional study of edge stress in graphene. *Physical Review B—Condensed Matter and Materials Physics* **78**, 073405 (2008).
49 Sun, P. *et al.* Unexpected catalytic activity of nanorippled graphene. *Proc. Natl. Acad. Sci. U. S. A.* **120**, e2300481120 (2023).
50 Hu, S. *et al.* Proton transport through one-atom-thick crystals. *Nature* **516**, 227-230 (2014).
51 Zhang, Z. *et al.* Rosin-enabled ultraclean and damage-free transfer of graphene for large-area flexible organic light-emitting diodes. *Nat. Commun.* **8**, 14560 (2017).
52 Dou, Y., Osipowicz, T. & van Kan, J. A. Breaking the 10 nm barrier using molecular ions in nuclear microprobes. *Ultramicroscopy* **253**, 113812 (2023).
53 Valiev, M. *et al.* NWChem: A comprehensive and scalable open-source solution for large scale molecular simulations. *Comput. Phys. Commun.* **181**, 1477-1489 (2010).
54 Becke, A. Density-functional thermochemistry. III. The role of exact exchange (1993) J. *Chem. Phys* **98**, 5648.
55 Paszke, A. *et al.* Automatic differentiation in pytorch. *In NeurIPS Autodiff Workshop* (2017).
56 Zhang, E. *et al.* Graphene rolls with tunable chirality. *Nat. Mater.* **24**, 377-383 (2025).
57 Xu, C. *et al.* Large-area high-quality 2D ultrathin Mo_2C superconducting crystals. *Nat. Mater.* **14**, 1135-1141 (2015).

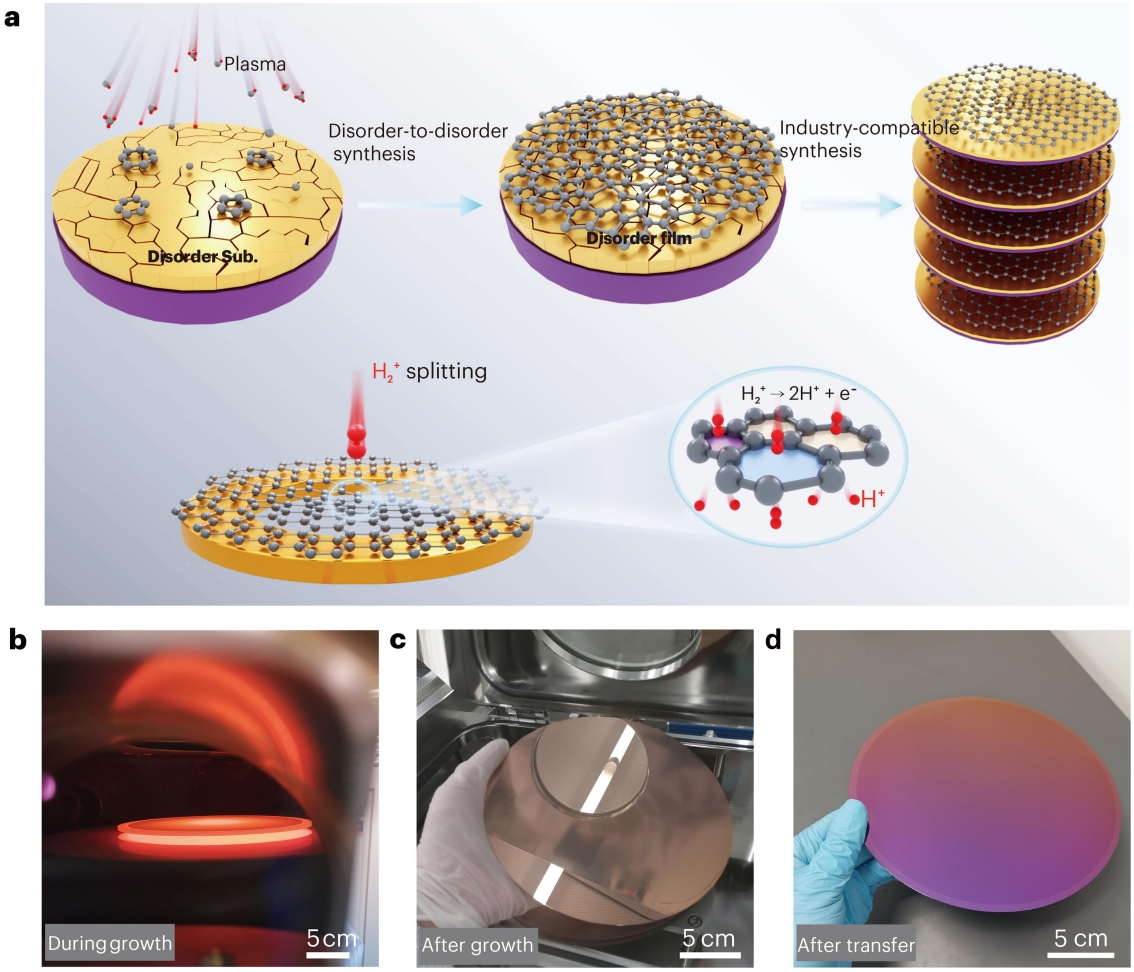


Fig. 1 | Disorder-to-disorder synthesis and application of wafer-scale UC-MAC. a, A schematic illustration for disorder-to-disorder synthesis of UC-MAC with tunable density of hexagonal and non-hexagonal rings towards the precise regulation of single H_2^+ splitting. **b-d**, the customized industry-compatible disorder-to-disorder growth system for fabricating an 8-inch wafer-scale UC-MAC: Photographs of (**b**) the synthesis process; (**c**) 8-inch UC-MAC on Disorder-Sub after growth; (**d**) 8-inch UC-MAC on SiO_2/Si after transfer.

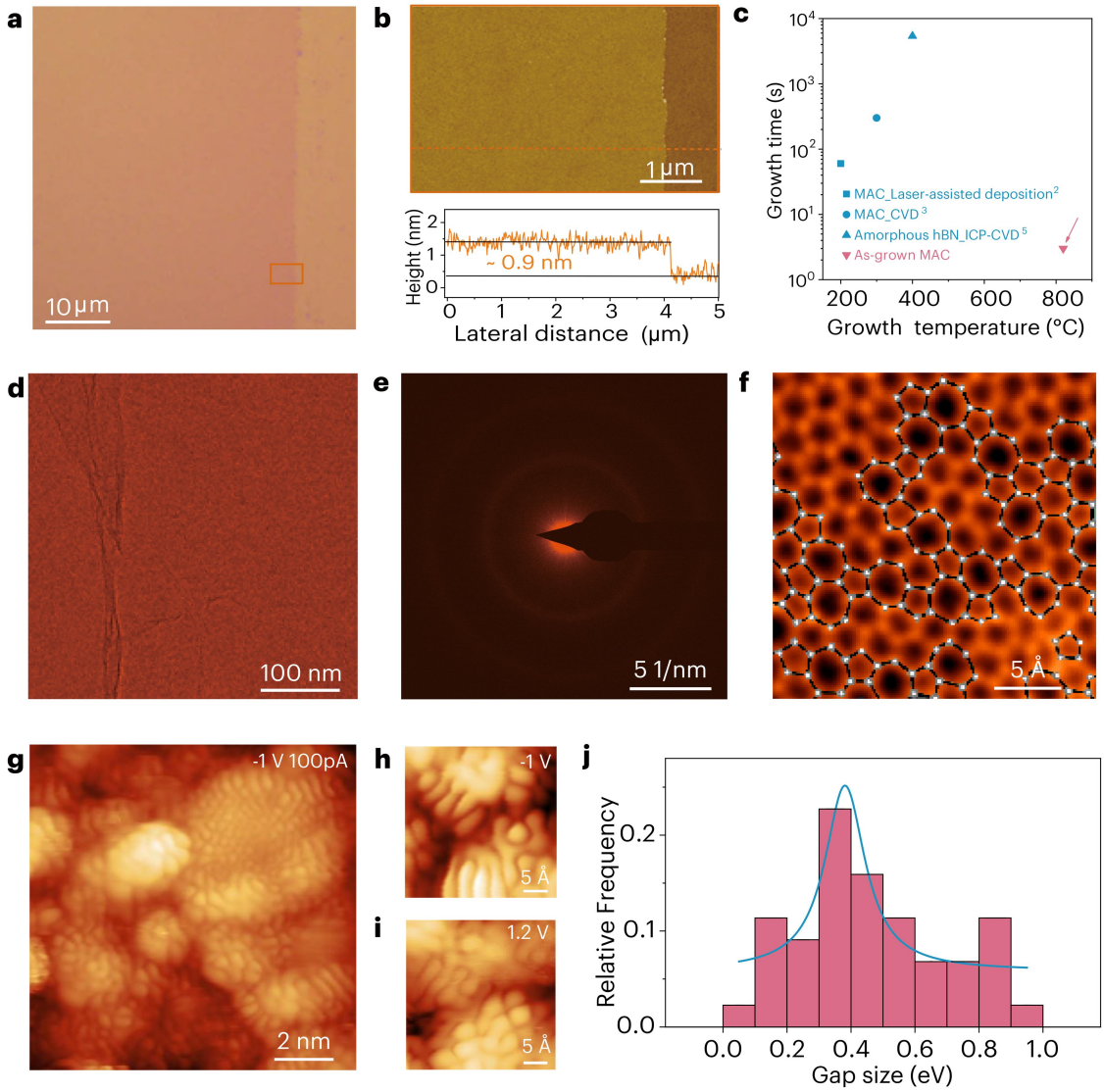


Fig. 2 | Atomic-scale structural and electronic characterizations of UC-MAC film. a, Optical microscopic image of as-grown UC-MAC transferred on a SiO_2/Si substrate, showing a homogenous and transparent optical contrast. **b**, the corresponding AFM image of the area marked by the brown square in (**a**), along with the height profile obtained along the brown-dashed line in (**b**), demonstrates an ultra-clean surface and monolayer thickness. **c**, Comparison of growth efficiency for UC- MAC with reported MACs[2,3] or amorphous hBN[5]. **d-e**, (**d**) A low-magnification TEM image reveals the 2D amorphous structure of UC-MAC, as proved by the corresponding SAED pattern shown in (**e**). **f**, An atomic-resolution STEM-ADF image of UC-MAC monolayer reveals the notable presence of non-hexagonal rings. **g**, A representative STM image of UC-MAC monolayer transferred onto HOPG substrate. Set point: -1.0 V, 100 pA. **h-i**, Bias-dependent zoom-in STM image of UC-MAC taken at both positive and negative sample biases. Set point: (**h**) -1.0 V, 100 pA; (**i**) 1.2 V, 100 pA. **j**, The statistical analysis of quasiparticle energy gaps measured by STS across over 50 different sample areas reveals a spatial variation, with an average value of 422±23 meV.

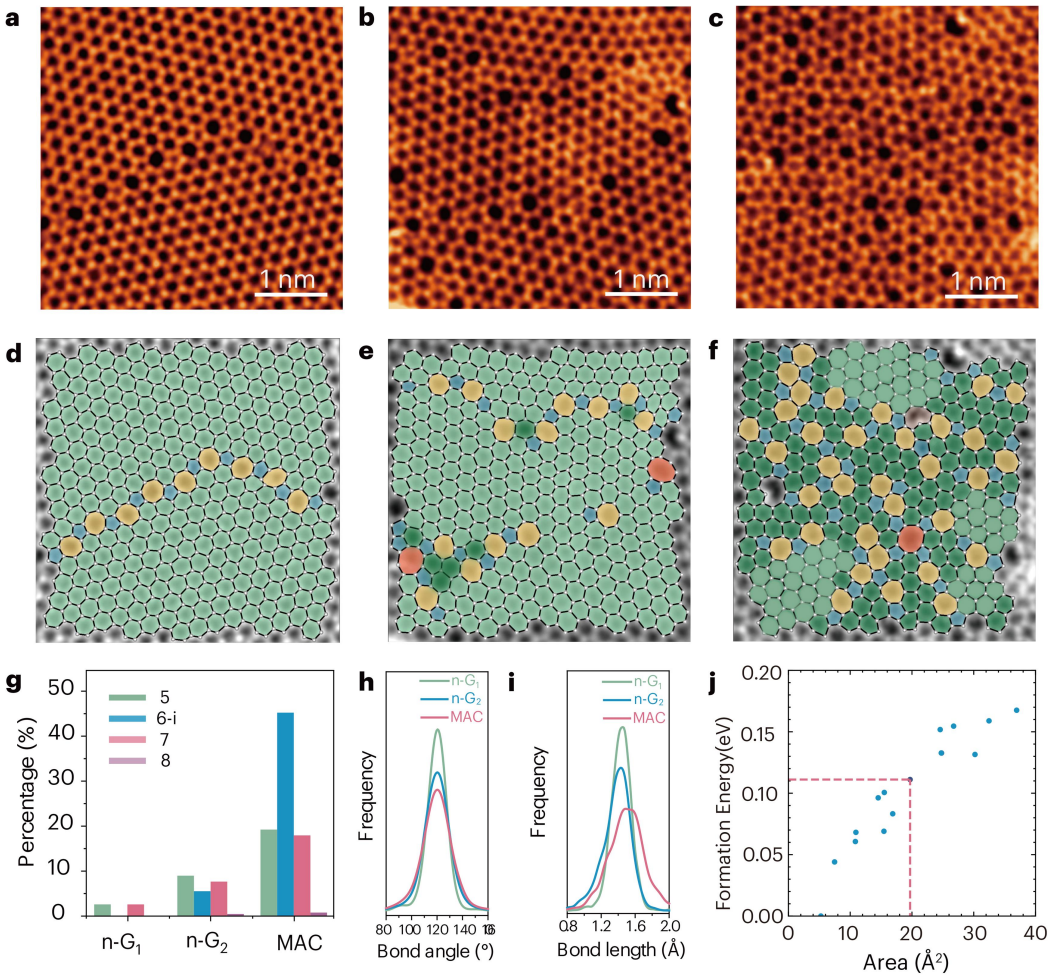


Fig. 3 | The growth and characterization of monolayer carbon with tunable density of non-hexagonal rings, ranging from mosaic n-G to UC-MAC. This is achieved through DTD synthesis of monolayer crabon on Cu Disorder-Subs using different ICP powers and growth time**. a–f**, Representative atomically-resolved STEM-ADF images and the corresponding colour-coded images for better visibility with averaged domain sizes ranging from hundreds of nanometers (n-G_2, **a**, **d**) to tens of nanometers (n-G_1, **b**, **e**), and UC-MAC (**c**, **f**). Non-hexagonal rings, including pentagonal, heptagonal, and octagonal carbon rings, are colored light blue, light orange, and pink, respectively. Hexagonal carbon rings within crystallite regions are highlighted in bright green, while those in isolated regions are shown in dark green. **g**, Statistics of the percentages of pentagons (5), hexagons (including crystallite hexagons (6-c), isolated hexagons (6-i)) and heptagons/octagons (7/8). **h-i,** Statistics of (**h**) bond-angle distributions and (**i**) bond-length distributions. **j**, Area of carbon ring/pore dependent formation energy in UC-MAC.

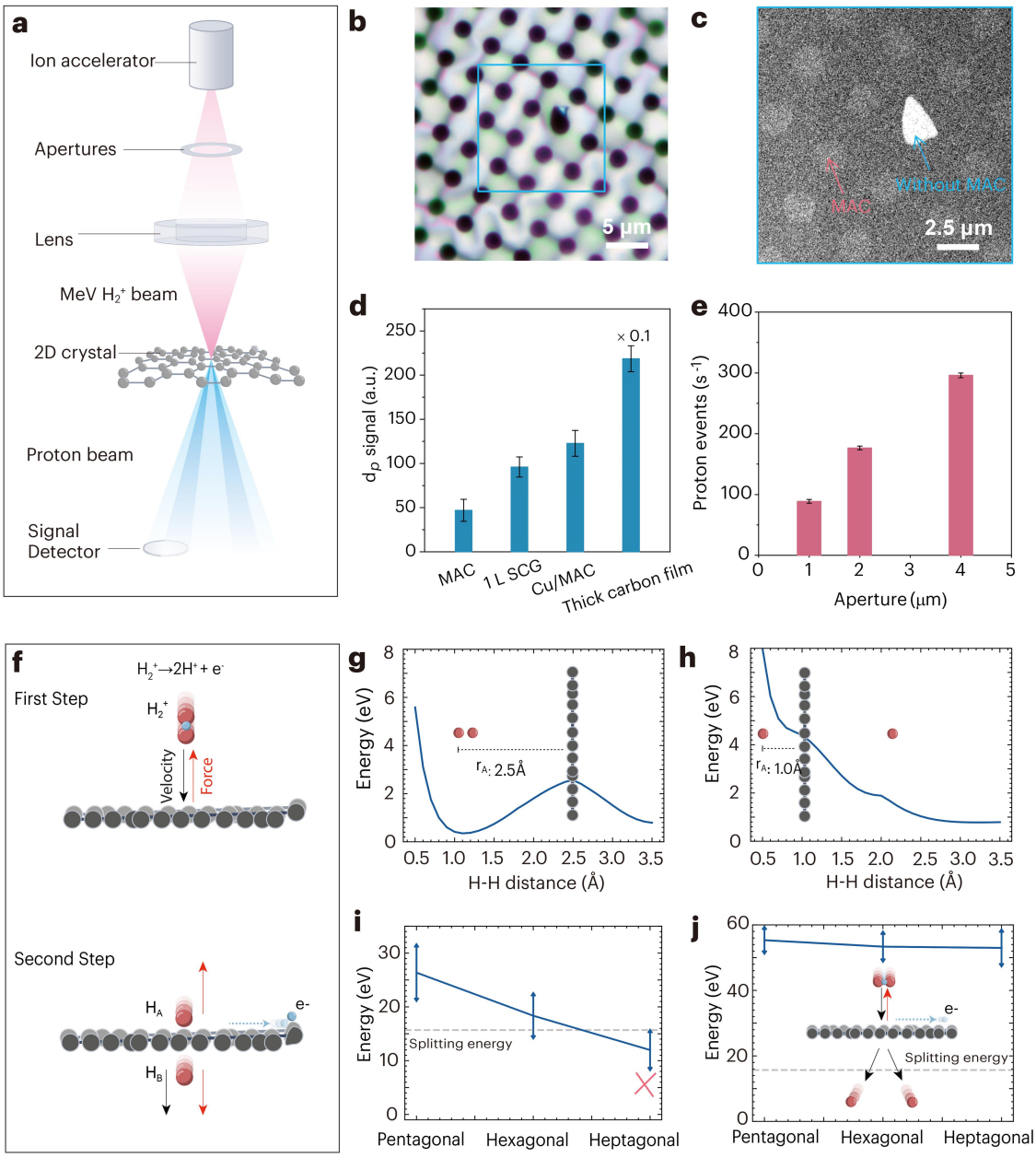
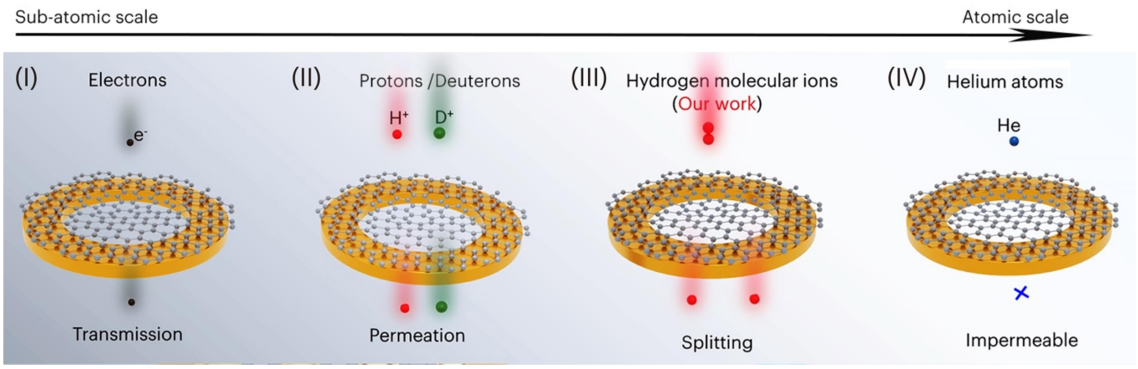
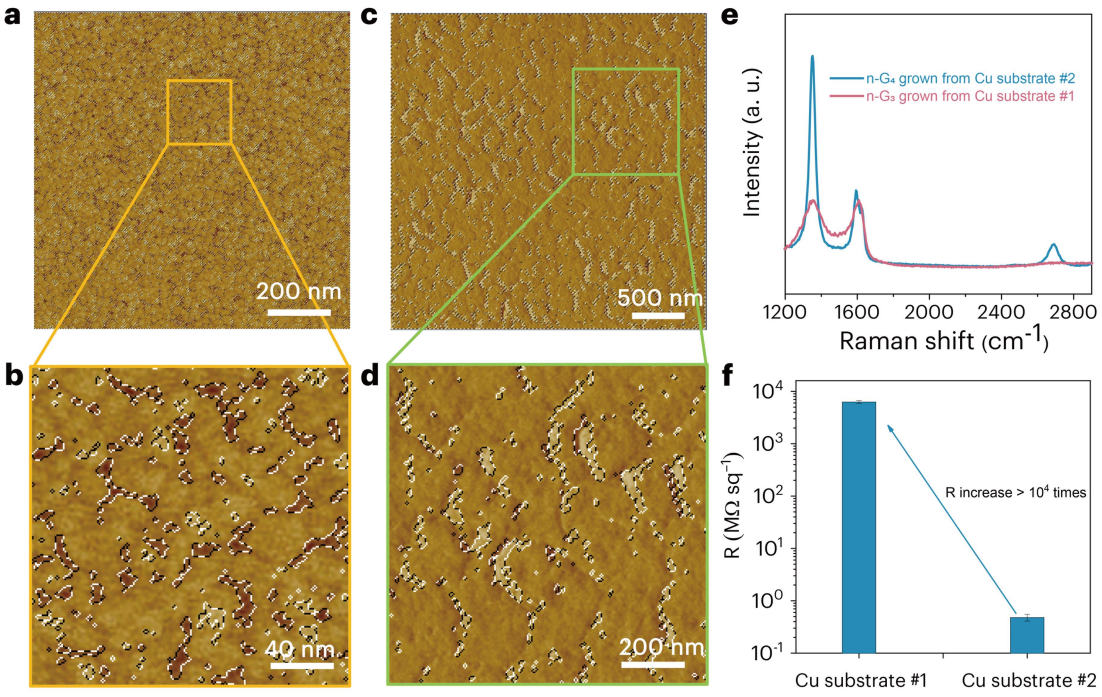


Fig. 4 | Splitting of hydrogen molecular ions on UC-MAC, non-clean MAC and SCG. a, Schematic diagram of high-energy ion nanobeams and bombardment of 2D crystals, and fragment protons are detected by a near-axis STIM. **b**, Optical microscopic image of free-standing UC-MAC on Au grid. **c**, Near-axis STIM image of the area marked by a Macaron blue square in (**b**), which can visualize the UC-MAC with an enhanced contrast compared to empty regions (marked by pink and Macaron blue arrows, respectively). **d**, Double-proton events for splitting of H_2^+ ions on UC-MAC, SCG, non-clean MAC decorated with metal impurities, and commercial thin carbon film (~8 nm) as a reference. One double-proton events (d_p) represents two protons signal detected from single H_2^+ ion splitting. **e**, Controlling the splitting rate of hydrogen molecular ion using UC-MAC. Error bars

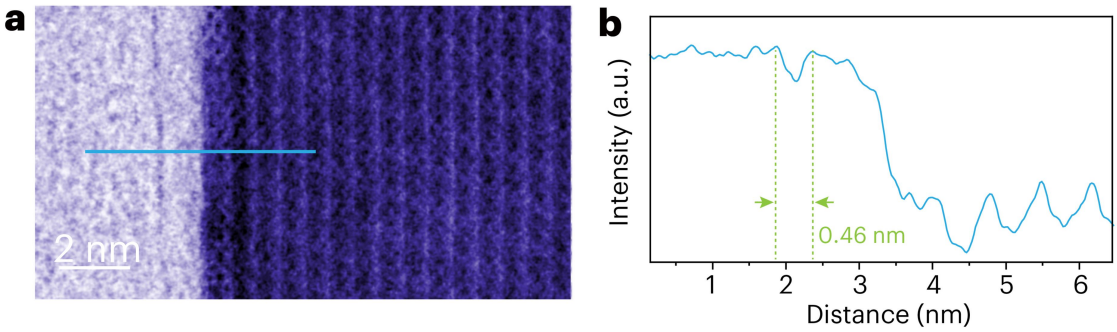
represent standard deviation (±SD) determined from 5 repeated measurements. **f**, Schematic diagram illustrating the travel of H_2^+ ion towards a 2D crystal plane showing the configuration before (first step) and after (second step) splitting of H_2^+ ions as it moves in the vertical configuration towards the 2D crystal. **g-h**, The computed energy profile of H_2^+ splitting (total energy of H_2^+ vs. H-H bond length) at given distance of (**g**) 2.5 Å and (**h**) 1.0 Å, measured from the backend H_A to the SCG/UC-MAC monolayer (r_A). **i-j**, The computed energy barrier for the second-step splitting of H_2^+, with the initial H_2^+ ion in the vertical configuration (**i**) or in the parallel configuration (**j**) toward the SCG/UC-MAC monolayer, when passing through either the hexagonal or non-hexagonal (pentagonal or heptagonal) rings (see inset in (**j**)). As a comparison, the computed splitting energy of gas-phase H_2^+ was ~15.6 eV and marked by the horizontal dashed line in gray color. The mean energy barrier was defined as the average value of the lower and upper limits of the computed energy barrier (See method). The red cross shown in (**i**) denotes the least favorable polygonal ring for H_2^+ splitting, i.e., when H_2^+ passing through a heptagonal ring in UC-MAC monolayer.



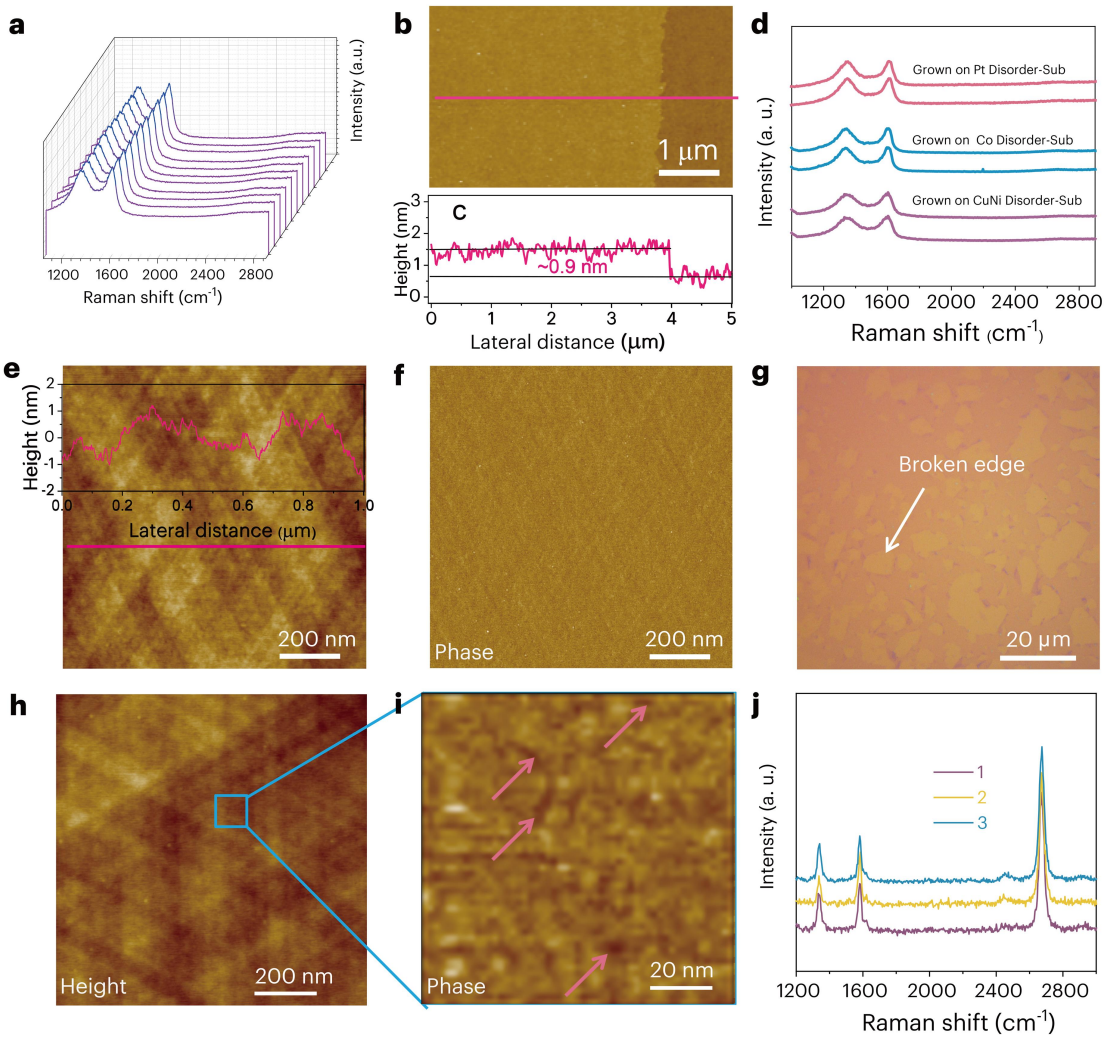
Extended Data Fig. 1 | Illustrating the subatomic species transport through atomically thin membranes. (**I**) Electrons, (**II**) Protons, (**III**) hydrogen molecular ion (our work) through atomically thin membranes; (**IV**) Helium atoms cannot pass through atomically thin membranes.



Extended Data Fig. 2 | Cu Disorder-Sub with different grain sizes for the synthesis of mosaic n-Gs. AFM phase images of Cu substrate with different sputtering parameters show nanograins embedded in main phase of Cu substrate. **a-b**, Cu substrate #1: ~2260±20 /um^2. **c-d**, Cu substrate #2: ~72±12 /um^2. Grain densities of the Disorder-Sub were calculated from statistical analysis of AFM phase images at three randomly selected regions. **e-f**, Raman spectra (**e**) and Resistance (**f**) of the growth of mosaic n-G with tuned non-hexagonal rings density by grown on different Cu substrates with different grain sizes under the same growth conditions. As confirmed in Extended Data **Fig. 2a-d**, there are numerous nanograins regions with different nanograins density in main Cu substrate, and the number of nanograins regions in Cu substrate #1 is 31 times that of Cu substrate #2. When graphene was grown under the same growth batch, compared with substrate 2, mosaic n-G_3 on Cu substrate #1 has a higher density of non-hexagonal rings, which show a decrease in the D peak and a disappearance of the 2D peak in the Raman spectra (Extended Data **Fig. 2e**). At the same time, the relative resistance of mosaic n-G_3 on Cu substrate #1 increased approximately 10,000 times larger compared to mosaic n-G_4 on Cu substrate #2 (Extended Data **Fig. 2f**).

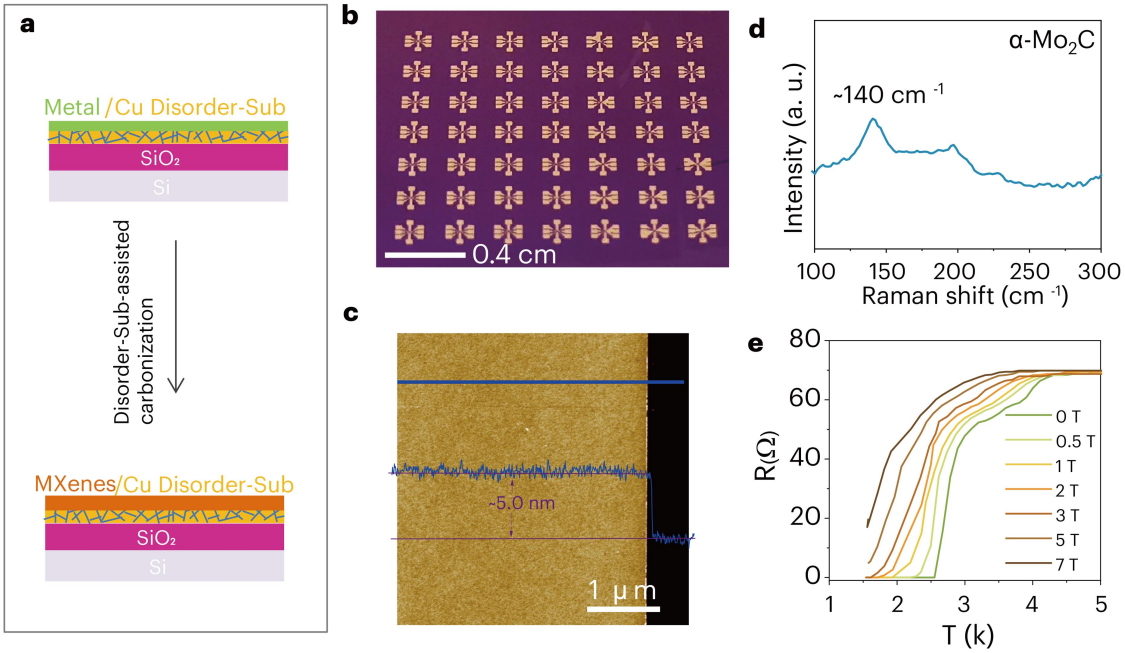


Extended Data Fig. 3 | STEM-ADF cross-sectional image of UC-MAC film with monolayer thickness. Cross-sectional STEM-ADF image of monolayer MAC (**a**) and the corresponding intensity line profile (**b**) along the Macaron blue line in (**a**). The measured thickness of UC-MAC is 0.46 nm, confirming its monolayer nature. During focused ion beam (FIB) milling, the MAC was protected by the beam-sensitive material $NbOBr_2$ to preserve the integrity of the monolayer UC-MAC.

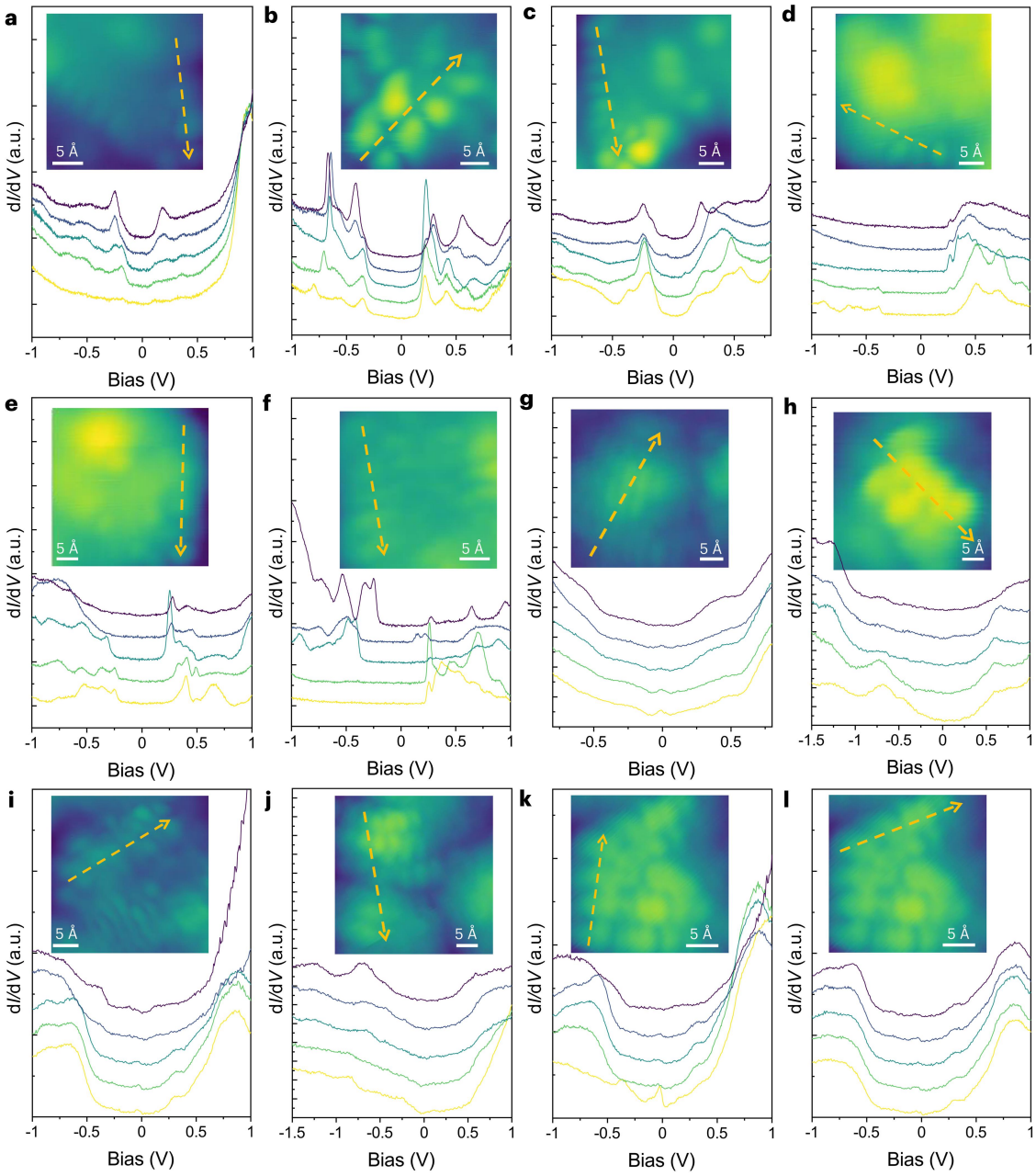


Extended Data Fig. 4 | Ultrafast growth and scalable growth by disorder-to-disorder synthesis. a-c, Raman spectra collected of the points at random intervals of 20 µm (**a**), AFM image (**b**) and the corresponding height profile (**c**) of ultrafast-grown UC-MAC on a SiO_2/Si substrate. Ultrafast growth of MAC is achieved within just 3 seconds, the minimum time limit of our deposition system, ensuring consistent and repeatable growth. **d,** Raman spectra of scalable growth of UC-MAC grown on different Disorder-Sub supports including Pt, Co, CuNi Disorder-Subs. **e-f,** AFM height image (**e**) and AFM phase image (**f**) of as-sputtered Cu(111) single crystal with high surface smoothness and single Cu(111) phase, consistent with the reported single Cu(111)[28,39]. **g,** Optical microscopic image of graphene on a SiO_2/Si substrate grown from a Cu(111) single crystal. The substrate is not fully covered by as-grown graphene film, even after extending the growth time to 100 seconds. The non-uniform contrast in (g) arises from the edges of partially grown graphene domains, which curled upward upon contact with the solution during the transfer process due to surface tension effects[56]. **h-j,** AFM height image (**h**), AFM phase image (**i**) and Raman spectrum (**j**) of as-gown graphene on Cu(111) single crystal. The bare Cu(111) exposed regions are marked by pink arrows (**i**). The AFM phase images indicate that graphene does not fully cover the

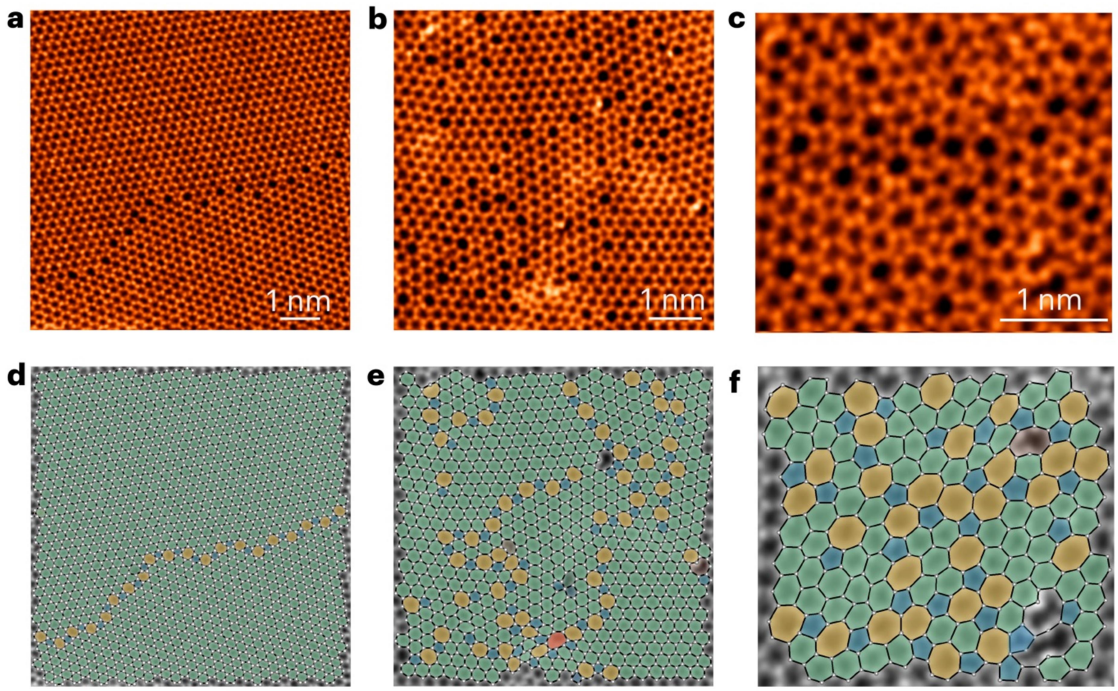
Cu(111) surface, leaving some regions of bare Cu(111) exposed (Extended Data **Fig. 4h-i**). Additionally, the presence of a defect-related D peak in the Raman spectrum further confirms this observation (Extended Data **Fig. 4j**).



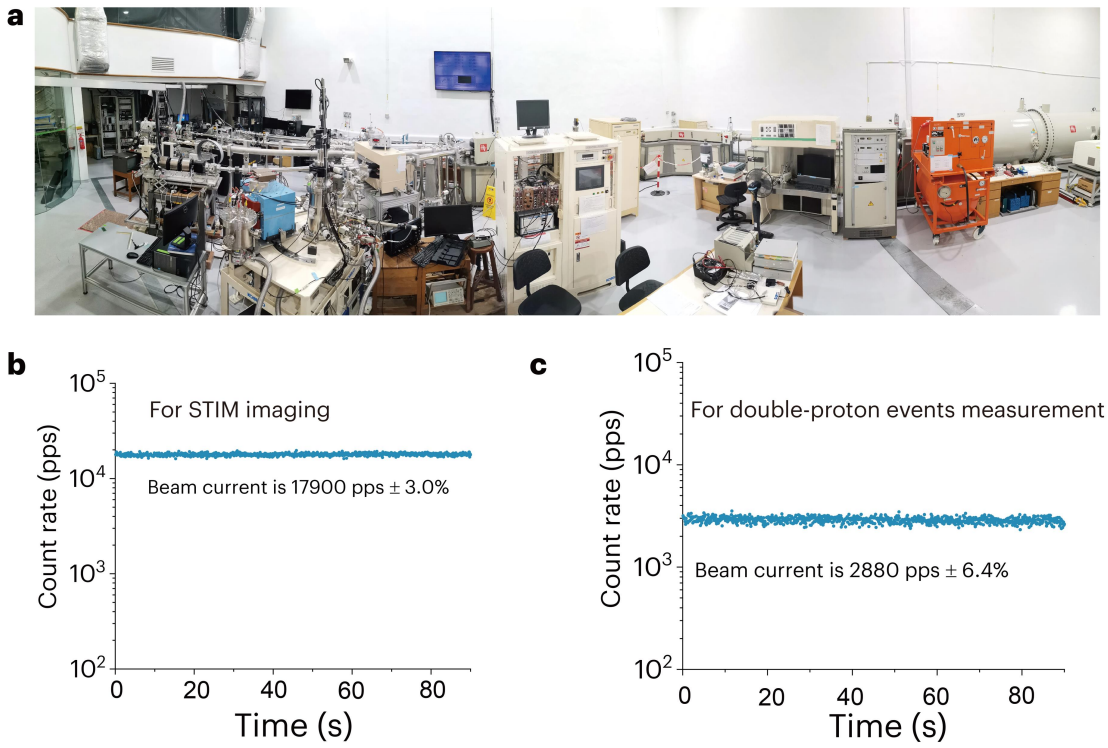
Extended Data Fig. 5 | Nanocrystalline transition metal carbides (TMCs) by disorder-to-disorder growth. a, The growth of nanocrystalline TMCs by Disorder-Sub-assisted carbonization. **b,** Hall bar device array of α-Mo_2C film. **c,** AFM image and the corresponding height profile (inset) of as-grown nanocrystalline α-Mo_2C film. **d-e,** Raman spectrum (**d**) and superconducting resistance transition of a 5 nm α-Mo_2C film (**e**) under an out-of-plane magnetic field. As shown in Extended Data **Fig. 5e**, the nanocrystalline α-Mo_2C film exhibit significantly higher diamagnetism (> 7 T) compared to α-Mo_2C single crystal (~ 1.5 T) result from high density of line defects of the former[31,57]. This disorder-to-disorder approach not only accelerates UC-MAC growth but also enhances the versatility and adaptability of the 2D materials growth technique, broadening its potential applications.



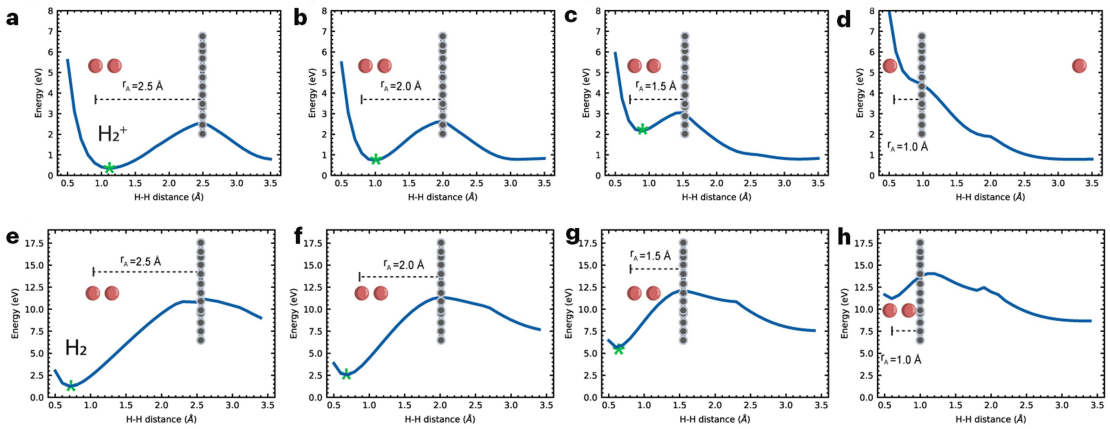
Extended Data Fig. 6 | Statistic analysis of the electronic properties of UC-MAC. Representative STM images of UC-MAC transferred onto HOPG substrate, along with multiple sets of line d*I*/d*V* spectra taken from over 12 different regions, along the line marked in the corresponding inset STM images.



Extended Data Fig. 7 | STEM-ADF images of mosaic n-Gs and UC-MAC samples grown in different batches confirm the controllability of the disorder-to-disorder growth process. a–f, Representative atomically-resolved STEM-ADF images and the corresponding colour-coded images for better visibility with averaged domain sizes from hundreds of nanometers (n-G_2, **a**, **d**) to tens of nanometers (n-G_1, **b**, **e**), and UC-MAC (**c**, **f**).



Extended Data Fig. 8 | Experimental platform for splitting of hydrogen molecular ions on UC-MAC, non-clean MAC and SCG. a, platform of high-energy ion nanobeam. **b-c,** Typical hydrogen molecular ion beam stabilities data for STIM imaging (**b**) and double-proton events measurement (**c**).



Extended Data Fig. 9 | Computed energy profiles (**a-d**) for the H_2^+ ion splitting and (**e-h**) for neutral H_2 molecule splitting at given distance (r_A) for backend H_A away from the graphene monolayer. Here, the H-H distance is used as the reaction coordinate for the molecular ion or molecule splitting in vertical configuration.

Supplementary Files

This is a list of supplementary files associated with this preprint. Click to download.

- Movie1Singlehydrogenmolecularionsplittingthroughhexagonsbybinarystepmodel.mp4
- Movie2Singlehydrogenmolecularionsplittingthroughhexagonsbylinearmodel.mp4
- Supportinginformation.pdf